Relaxation Processes in Dipole-Coupled Nitrogen-Vacancy Centers in Zero Field: Application in Magnetometry

C. Pellet-Mary,[1] M. Perdriat,[1] P. Huillery,[2] and G. Hétet[1,*]

[1] *Laboratoire De Physique de l'École Normale Supérieure, École Normale Supérieure, PSL Research University, CNRS, Sorbonne Université, Université Paris Cité , 24 rue Lhomond, Paris 75231 Cedex 05, France*
[2] *Université Rennes, INSA Rennes, CNRS, Institut FOTON - UMR 6082, Rennes F-35000, France*

(Received 25 July 2022; revised 18 June 2023; accepted 28 August 2023; published 21 September 2023)

We study relaxation processes in dipolar-coupled negatively charged nitrogen-vacancy (N-V^-) centers close to zero field. Specifically, we uncover regimes where flip-flop and double-flip processes, as well as mixing induced by local electric fields, play a significant role in N-V–N-V cross relaxation. Our results are relevant for understanding decoherence in many-body spin systems, as well as for high-sensitivity magneto- and electrometry with long-lived interacting solid-state spins. As a proof of principle, we present an orientation and microwave-free magnetometer based on cross relaxation.

DOI: 10.1103/PhysRevApplied.20.034050

The electronic spin properties of the negatively charged nitrogen-vacancy (N-V^-) center in diamond have given rise to a wealth of applications in nanoscale sensing and quantum information science thanks, in part, to the possibility to optically polarize and read-out its spin state under ambient conditions [1]. In particular, ensembles of N-V centers are widely studied for their enhanced magnetic-field-sensing capabilities [2–7] and as pristine platforms for observing many-body effects [8–11]. When the N-V spin concentration reaches ppm values, spin depolarization, or cross relaxation (CR), takes place through a very rich many-body dynamics associated with disorder [12]. These mechanisms limit the efficiency of typical microwave-based N-V magnetometers, but quantum control techniques can be combined to surpass this interaction limit [13]. Furthermore, CR mechanisms can be used as a tool for magnetic field sensing [14,15]. Spectral features in the photoluminescence (PL) indeed appear when the magnetic field crosses specific crystal planes where dipolar interactions are enhanced, leading to CR [12,14–17]. The projected sensitivity of such magnetometers lies in the tens of $\mathrm{pT}/\sqrt{\mathrm{Hz}}$ [14], on a par with the most sensitive microwave-based N-V magnetometers [18,19].

Cross-relaxation features close to zero magnetic field have also been observed and can be deployed for higher-sensitivity microwave-free magnetometry [20,21]. The CR contrast was shown to be much larger in the zero-field limit [22,23], but all of the relaxation mechanisms have not been identified there. Here, we study dipolar-relaxation processes in ensembles of N-V centers in the presence of small transverse electric and magnetic fields. Specifically, employing magnetic field scans along crystalline directions, we find regimes where flip-flop and double-flip processes, as well as mixing induced by local electric fields, play a role. We also present an orientation- and microwave-free magnetometer that makes use of these mechanisms in the dipolar interaction between N-V centers.

The processes that lead to depolarization in strongly coupled spin-1 systems are depicted in Fig. 1. Flip-flop processes involving coupling between spins with identical or different orientations, or "classes," are depicted in the top-right panel. They have already been shown to play a dominant role in dense ensembles of N-V centers, when $B \gtrsim 30$ G: tuning the difference, Δ, between the different N-V centers' spin states indeed result in a strong T_1 reduction [12]. We show here that double-flip up and down, also known as flip-flip processes, as well as mixing induced by local electric fields (cf. two bottom panels) can also give a significant contribution to spin depolarization close to zero field.

The manuscript is structured as follows. In Sec. I, we present the experimental setup employed to detect the spin of the N-V centers via optically detected magnetic resonance (ODMR) as well as the ODMR response when the magnetic field is tuned to specific diamond crystal planes. In Sec. II, we provide a theoretical framework to model the spin-depolarization mechanism under small magnetic fields. In Sec. III, we present experimental observations of spin depolarization and compare them with theoretical expectations. Lastly, in Sec. IV, we use the zero-field feature to demonstrate and characterize a microwave-free magnetometry protocol.

*gabriel.hetet@ens.fr

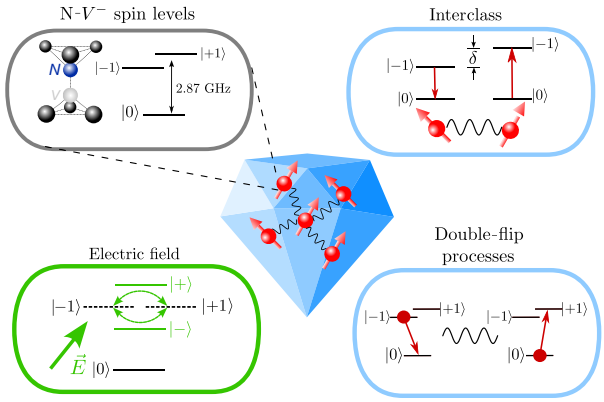

FIG. 1. Schematics showing a diamond with interacting spins (central picture) as well as three processes that account for dipolar relaxation: flip-flop processes involving two different classes of N-V centers, local electric field mixing, and double-flip processes where two units of spin angular momentum are exchanged.

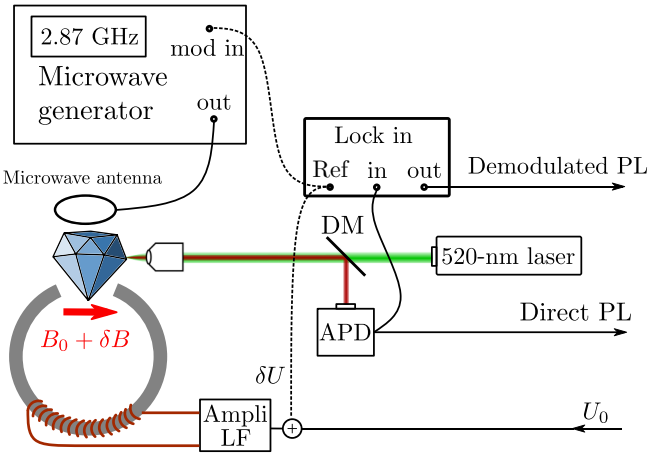

FIG. 2. Experimental setup. Diamonds are subjected to a green laser and a magnetic field in the hundreds of gauss range. PL in the μW range passes through a dichroic mirror (DM) and is detected on an avalanche photodiode (APD).

I. OPTICAL DETECTION OF ENSEMBLE OF N-V SPINS

The electronic spin of the N-V center is a spin-1 system in the electronic ground state (see Fig. 1, top-left panel), which can be optically polarized in the $|m_s = 0\rangle$ state using a green laser. The $|m_s = \pm 1\rangle$ spin states are separated from the $|m_s = 0\rangle$ state by the so-called zero-field splitting (ZFS), $D = (2\pi)2.87$ GHz. PL in the $|m_s = 0\rangle$ state is larger than in the $|m_s = \pm 1\rangle$ states [1]. When a microwave is applied at a frequency D, the PL is then reduced [24,25]. This is the essence of the ODMR technique.

A. Experimental setup

Figure 2 shows the experimental setup used for all the experiments presented herein. The optical polarization and read-out of the spins is done by focusing a green laser on the diamond sample with an objective lens (NA = 0.65), and collecting the backscattered red fluorescence from the N-V center on an APD (Thorlabs APD410A). The laser is filtered out using a dichroic mirror and a notch filter. The N-V^0 fluorescence is filtered out using an additional 645-nm long-pass filter.

The laser is a Picoquant PDL 800-D with a 520-nm LDH laser head, providing pulses of 40 ps at a rate of 20 MHz, with an average power of 0.5–5 mW. These fast pulses serve no purpose in the actual experiment. Similar experiments were performed using a continuous 532-nm laser and no difference in the spin response was observed. This laser was used solely because of its high amplitude stability, which improved the N-V magnetometer sensitivity. The magnetic field is provided by a homemade electromagnet composed of a C-shaped iron core and copper wires. The magnet is mounted on two mechanical rotation stages, allowing control of the polar and azimuthal angles of the magnetic field within a fraction of a degree, and is powered through a low-frequency amplifier (Leybold power function generator 522 63). The microwave field is generated by a Rhode & Shwarz SMB-100A instrument and is applied to the spin by a handmade current-carrying loop. The microwave field is gated by a Mini-circuits ZASWA-2-50DRA+ switch controlled externally and amplified by a Mini-circuits ZHL-5W-422+ amplifier. A lock-in amplifier (SRS SR830 DSP) is used either to detect ODMR or for CR-based magnetometry with low noise. We modulate the microwave amplitude for ODMR measurements or to add an oscillatory magnetic field for the magnetometry protocol. In both cases, we use a modulation frequency of about 1 kHz and demodulate the APD signal using the lock-in amplifier.

To certify the sample independence of the effects discussed herein, we employ several samples of different origin, most of them with a large concentration of N-V centers. Their properties and origin are listed in Table I.

Typical ODMR measurements are shown in Fig. 3 under zero magnetic field and under a magnetic field of 50 G, when focusing on a single N-V class. Note that these data have been taken using an amplitude modulation at 1 kHz on the microwave tone and using the lock-in amplifier for demodulation and filtering.

As can be see in Fig. 3(a), under zero applied magnetic field, the energy of the $\{|+1\rangle, |-1\rangle\}$ states differs. Three possible processes can cause this splitting: local electric fields, crystal strain, and local magnetic fields. Of these three causes, only the electric field can explain the shape of the ODMR line that is observed [26]. Indeed, a random local magnetic field would produce a single broadened line, while crystal strain would shift the ZFS

TABLE I. Description of the diamond samples used in this study. Labels *i* indicate the specific sample employed in the experiment. AN, Adamas Nanotechnology. In the HPHT samples, the size is the diamond diameter.

Item name	Diamond size	[N-V^-]	[N] (ppm)	Origin
HPHT-150-*i*	150 μm	≈ 3 ppm	≈ 100	AN MDNV150umHi
HPHT-15-*i*	15 μm	≈ 3 ppm	≈ 100	AN MDNV15umHi
HPHT-1-1	1 μm	≈ 3 ppm	≈ 100	AN MDNV1umHi
CVD-1	4×4 mm^2 and a few mm thick	≈ 50 ppb	<1	Element 6, optical grade
CVD-2	4×4 mm^2 and a few mm thick	≈ 4 ppm	≈ 25	Irradiated and annealed [3]

by the same order of magnitude as the splitting between the levels, which would merge the two transitions onto a single line. Due to the large difference between the longitudinal and transverse electric field susceptibilities ($d_\parallel = 0.35$ Hz cm/V and $d_\perp = 17$ Hz cm/V [27]), a random local electric field can, on average, cause a splitting that is much stronger than the ZFS shift and result in a two-peak spectrum centered at 2.87 GHz. In our model for dipole-dipole coupling under small magnetic fields, we therefore neglect the contributions of strain, local magnetic fields, and longitudinal electric fields.

In the absence of an external magnetic field, the symmetry of the Hamiltonian in the x-y plane allows us to pick the x direction along the electric field. The eigenstates of $\mathcal{H}_s$ then become $\{|0\rangle, |+\rangle = (|+1\rangle + |-1\rangle)/\sqrt{2}, |-\rangle = (|+1\rangle - |-1\rangle)/\sqrt{2}\}$. In the presence of a magnetic field at an angle θ with respect to the N-V axis, we denote the Hamiltonian eigenstates as $\{|g\rangle, |d\rangle, |e\rangle\}$, in ascending order of energy. Figure 4 quantifies how close the $|e\rangle$ state is to the $|+1\rangle$ and $|+\rangle$ states as a function of the external magnetic field and angle θ. A similar analysis for the $|d\rangle$, $|-1\rangle$ and $|-\rangle$ states shows similar results, while $|g\rangle$ is close to $|0\rangle$ for $B < 100$ G. This result shows that the $\{|0\rangle, |+\rangle, |-\rangle\}$ basis is a good eigenbasis for magnetic fields smaller than a few gauss, except in the case of a pure transverse magnetic field, where the $\{|0\rangle, |+\rangle, |-\rangle\}$ basis remains a good basis up to about 200 G. These considerations are essential to understand the role of electric fields in the N-V spin depolarization under small magnetic fields.

From the resonance linewidths measured in a magnetic field, as shown in Fig. 3(b), we can extract decoherence times, T_2^*, in the hundreds of nanosecond range, limited by the coupling between N-V centers and the fluctuating spins of substitutional nitrogen atoms (also called P_1 centers). We can neglect the hyperfine structure of the N-V center under these conditions. Indeed, the inhomogeneous broadening of the ODMR transitions in all our samples is in the tens of MHz range, while the hyperfine splitting between the electronic spin and the nuclear spin of the natural abundance nitrogen isotope, ^{15}N, is 2.14 MHz.

We then consider the following spin Hamiltonian for the N-V^- ground state:

$$\mathcal{H}_s/\hbar = DS_z^2 + d_\perp E_x(S_y^2 - S_x^2) + d_\perp E_y(S_xS_y + S_yS_x) + \gamma_e \mathbf{B}\cdot\mathbf{S}, \quad (1)$$

where $\gamma_e = 2.8$ MHz/G is the gyromagnetic ratio of the electron and **B** is the external magnetic field.

Crucial to this study, as we shall see, is the possibility to tune the number of degenerate N-V-center classes. We show in Fig. 5 five different ODMRs, where the magnetic field is tuned to specific crystal planes to achieve different degeneracy conditions between N-V classes. These different configurations yield different spin-relaxation rates, as we now discuss.

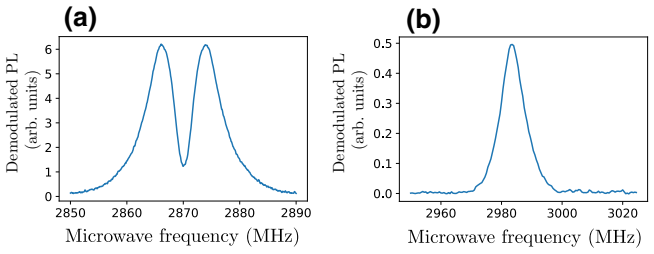

FIG. 3. Typical ODMR measurements (a) under zero magnetic field and (b) under a magnetic field of 50 G when focusing on a single N-V class. Sample HPHT-150-1.

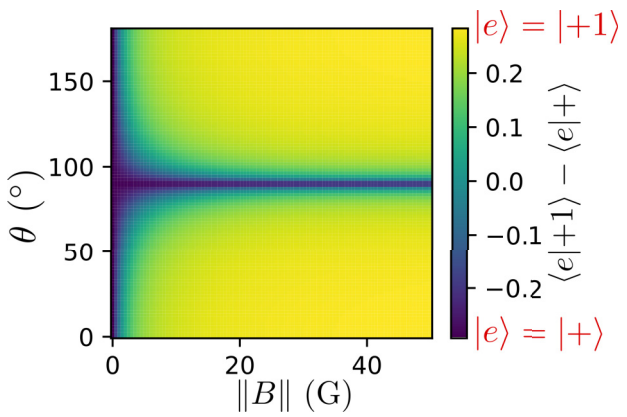

FIG. 4. Numerical simulations showing overlap between the second-excited-state, $|e\rangle$, and the states $|+1\rangle$ and $|+\rangle$, as a function of the magnetic field amplitude and angle θ with respect to the N-V axis. Value of $d_\perp E_\perp = 4$ MHz was chosen.

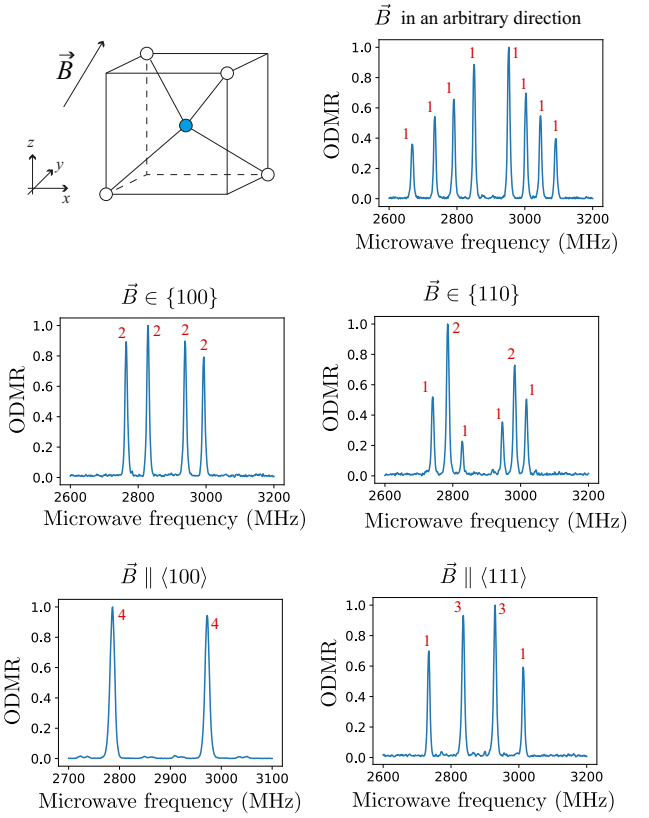

FIG. 5. ODMR spectra for different orientations of the magnetic field. Red numbers represent the number of degenerate classes for each line of the spectrum.

II. SPIN-DEPOLARIZATION THEORETICAL BACKGROUND

Here, we discuss the results of the fluctuator model developed in Ref. [28], which is extended to include double-flip processes and the role of local electric fields, to describe the N-V spin relaxation.

A. N-V-Fluctuator model

In the fluctuator model, the N-V^- centers in the diamond are divided into two categories: "normal" N-V centers (simply called N-V), which, in the absence of dipole-dipole coupling would have a phonon-limited T_1 ($T_1^{\text{N-}V} \sim$ ms), and "fluctuators," which have the same energies as the N-V centers in the ground state but a faster depolarization mechanism, such that their lifetime is $T_1^f < 100$ ns. Having such a short lifetime, the fluctuators are almost unpolarized by the green laser, making them invisible in the standard optical N-V measurement protocol (T_1, ODMR, etc.) The exact cause of this fast depolarization is unknown.

Assuming a homogeneous distribution of fluctuators in the bulk of the crystal, Choi *et al.* [28] show that the fluctuators create an additional decay channel for the normal N-V population, through dipole-dipole interactions, characterized by decay rate γ, which follows the probability distribution

$$\rho(\gamma) = \frac{e^{-1/(4\gamma T)}}{\sqrt{4\pi\gamma^3 T}}. \tag{2}$$

The timescale, T, is

$$\frac{1}{T} = \left(\frac{4\pi n_f J_0 \bar{\eta}}{3}\right)^2 \frac{\pi}{\gamma_f}, \tag{3}$$

where n_f is the fluctuator density in the crystal in nm^{-3}, $J_0 = 52\,\text{MHz}\,\text{nm}^3$ is the characteristic dipole-dipole strength between two electronic spins, γ_f is the fluctuator's intrinsic decay rate, and $\bar{\eta}$ is a dimensionless number that characterizes the average dipole-dipole interaction between the N-V centers and the fluctuators (resonance conditions, relative orientations, etc.; further details are given below).

After turning OFF the green laser, the normalized photoluminescence of the ensemble of N-V centers then follows

$$P(t) = \int_0^\infty \rho(\gamma)\, e^{-\gamma t} d\gamma = e^{-\sqrt{t/T}}, \tag{4}$$

which corresponds to a depolarization rate characterized by stretched-exponential behavior.

B. Dipole-dipole Hamiltonian between a single N-V and a fluctuator

Let us consider the Hamiltonian of an N-V center interacting with a fluctuator:

$$\mathcal{H}_{\text{tot}} = \mathcal{H}_1 + \mathcal{H}_2 + \mathcal{H}_{dd}. \tag{5}$$

$\mathcal{H}_1$ and $\mathcal{H}_2$ are the single-particle Hamiltonians of N-V and the fluctuator, as described by Eq. (1), and $\mathcal{H}_{dd}$ is the dipole–dipole-interaction Hamiltonian between the two spins.

We consider the spin operators $\mathbf{S}_1$ and $\mathbf{S}_2$ in the N-V basis: the z orientation of the S_z operator is thus chosen along the N-V axis of each spin. In the presence of a longitudinal magnetic field, the direction of $\hat{z}$ is chosen, such that $\mathbf{B} \cdot \hat{z} > 0$, and the $\hat{x}$ direction is chosen along the transverse magnetic or electric field, whichever dominate the single-spin Hamiltonian in the transverse plane. These choices imply that there will be two distinct Cartesian bases, $\{\hat{x}_1, \hat{y}_1, \hat{z}_1\}$ and $\{\hat{x}_2, \hat{y}_2, \hat{z}_2\}$, to parametrize the two spin directions.

The dipole-dipole Hamiltonian can then be decomposed as

$$
\begin{aligned}
-\frac{\mathcal{H}_{dd}}{J_0/r^3} &= 3\left(\mathbf{S}_1\cdot\hat{u}\right)\left(\mathbf{S}_2\cdot\hat{u}\right)-\mathbf{S}_1\cdot\mathbf{S}_2\\
&=\left[3(\hat{u}\cdot\hat{x}_1)(\hat{u}\cdot\hat{x}_2)-\hat{x}_1\cdot\hat{x}_2\right]S_x^1S_x^2\\
&\quad+\left[3(\hat{u}\cdot\hat{y}_1)(\hat{u}\cdot\hat{y}_2)-\hat{y}_1\cdot\hat{y}_2\right]S_y^1S_y^2\\
&\quad+\left[3(\hat{u}\cdot\hat{x}_1)(\hat{u}\cdot\hat{y}_2)-\hat{x}_1\cdot\hat{y}_2\right]S_x^1S_y^2\\
&\quad+\left[3(\hat{u}\cdot\hat{y}_1)(\hat{u}\cdot\hat{x}_2)-\hat{y}_1\cdot\hat{x}_2\right]S_y^1S_x^2\\
&\quad+\left[3(\hat{u}\cdot\hat{z}_1)(\hat{u}\cdot\hat{z}_2)-\hat{z}_1\cdot\hat{z}_2\right]S_z^1S_z^2,\\
&\quad+\mathcal{H}_{\text{other}},
\end{aligned}
\tag{6}
$$

where $J_0=(\mu_0\gamma_e^2\hbar^2)/4\pi=(2\pi)52\ \text{MHz}\,\text{nm}^3$; $\mathbf{r}=r\hat{\mathbf{u}}$ is the distance between the two spins. $\mathcal{H}_{\text{other}}$ contains terms of the form $S_x^iS_z^j$ and $S_y^iS_z^j$, which couple states that are far from resonance and are thus neglected here.

C. Flip-flops in the $\{|0\rangle, |+1\rangle, |-1\rangle\}$ magnetic basis

We first consider the case, treated in Ref. [28], where the longitudinal magnetic field is strong enough for the single-spin Hamiltonian eigenstates of both spins to be close to $\{|0\rangle, |+1\rangle, |-1\rangle\}$. The states $|+1\rangle$ and $|-1\rangle$ are nondegenerate, so only the matrix elements $\langle\pm1,0|\mathcal{H}_{dd}|0,\pm1\rangle$, describing flip-flops, are nonzero.

Following the notation in Ref. [28], we introduce the dimensionless factor η, which is defined as

$$
\eta^2=\frac{1}{3}\left|\langle\pm1,0|\frac{\mathcal{H}_{dd}}{J_0/r^3}|0,\pm1\rangle\right|^2\frac{4\gamma_f^2}{(\omega_f-\omega_{\text{N-}V})^2+4\gamma_f^2},
\tag{7}
$$

where γ_f is the fluctuator lifetime, $\omega_f/2\pi$ is the transition frequency of the fluctuator, and $\omega_{\text{N-}V}/2\pi$ is the N-V transition frequency. The $\bar{\eta}$ factor in Eq. (3) is the average of η over all orientations and angular positions of the fluctuators.

Assuming that the fluctuators are evenly distributed among all four classes of N-Vs and decomposing the $\mathbf{r}$ vector in the spherical basis (r,θ,ϕ), we can write $\bar{\eta}$ as

$$
\begin{aligned}
\bar{\eta}=\frac{1}{4}\sum_{i=1}^{4}\int_\theta\int_\phi\int_{\omega_f}\int_{\omega_{\text{N-}V}}&|\eta(\mathbf{u},i,\omega_{\text{N-}V},\omega_f)|\,d\Omega\\
&\times\rho(\omega_{\text{N-}V})d\omega_{\text{N-}V}\,\rho^i(\omega_f)d\omega_f,
\end{aligned}
\tag{8}
$$

where $d\Omega=\sin\theta d\theta d\phi$, $\rho(\omega_{\text{N-}V})$ is the distribution of angular frequencies of the probed N-V centers, and $\rho^i(\omega_f)$ is the distribution of angular frequencies for the fluctuators of class i.

Under these hypotheses, we find that there are three possible scenarios where the N-V and fluctuators are resonant.

(i) N-V *and fluctuator are from the same class*. The angle $\widehat{z_1z_2}=0$. This situation always occurs experimentally, regardless of the magnetic field angle and amplitude. We can compute $\bar{\eta}$ analytically and find

$$
\begin{aligned}
\bar{\eta}_{\text{same}}&=\frac{1}{4}\int_\theta\int_\phi|\eta(\mathbf{u},\widehat{z_1z_2}=0,\omega_{\text{N-}V}=\omega_f)|\,d\Omega,\\
&=\frac{1}{4}\times\sqrt{\frac{1}{3}}\times\frac{2}{3\sqrt{3}}\approx5.5\times10^{-2}.
\end{aligned}
\tag{9}
$$

(ii) N-V *and fluctuator form an angle* $\widehat{z_1z_2}=\arccos(1/3)\approx70.5^\circ$. This is the case when the magnetic field lies in the {100}-crystalline-plane family. Numerical simulations yield $\bar{\eta}_{\text{close}}\approx1/4\times\sqrt{1/3}\times0.65\approx9.4\times10^{-2}$.

(iii) N-V *and fluctuator form an angle* $\widehat{z_1z_2}=\arccos(-1/3)\approx109.5^\circ$. This takes place when the magnetic field lies in the {110}- or $\{1\bar{1}0\}$-crystalline-plane family. Numerically, simulations give $\bar{\eta}_{\text{far}}\approx1/4\times\sqrt{1/3}\times0.83\approx1.2\times10^{-1}$. This last case was not considered in Ref. [28].

The computed values of $\bar{\eta}^2$ normalized to $\overline{\eta_{\text{same}}}^2$ are listed in Table II for various magnetic field orientations. The largest depolarization is predicted for $\mathbf{B}\parallel\langle100\rangle$, where all four classes are resonant.

TABLE II. Description of the magnetic field orientation (see Fig. 5 for the corresponding ODMR), microwave selection, and the corresponding $\bar{\eta}$ and $\bar{\eta}^2/\bar{\eta}^2_{\text{same}}$ values. The isolated class case corresponds to a class that is only resonant with a fluctuator of the same orientation.

Magnetic field	Microwave selection	$\bar{\eta}$	$(\bar{\eta}/\overline{\eta_{\text{same}}})^2$
Random orientation	All isolated classes	$\bar{\eta}_{\text{same}}$	1
$\mathbf{B}\in\{110\}$	Two isolated classes	$\bar{\eta}_{\text{same}}$	1
	Two degenerate classes	$\bar{\eta}_{\text{same}}+\bar{\eta}_{\text{far}}$	10.0
$\mathbf{B}\in\{100\}$	Two pairs of degenerate classes	$\bar{\eta}_{\text{same}}+\bar{\eta}_{\text{close}}$	7.2
$\mathbf{B}\parallel\langle111\rangle$	Isolated class (parallel to $\mathbf{B}$)	$\bar{\eta}_{\text{same}}$	1
	Triply degenerate classes	$\bar{\eta}_{\text{same}}+2\bar{\eta}_{\text{far}}$	28.4
$\mathbf{B}\parallel\langle100\rangle$	Quadruple resonance	$\bar{\eta}_{\text{same}}+2\bar{\eta}_{\text{close}}+\bar{\eta}_{\text{far}}$	42.8

D. Flip-flops in the $\{|0\rangle, |+\rangle, |-\rangle\}$ nonmagnetic basis

When the single-spin Hamiltonian of the N-V center is dominated by the electric field or by the transverse magnetic field in the $\gamma_e B_\perp \ll D$ regime, the eigenbasis of the N-V Hamiltonian is close to $\{|0\rangle, |+\rangle = (|+1\rangle + |-1\rangle)/\sqrt{2}, |-\rangle = (|+1\rangle - |-1\rangle)/\sqrt{2}\}$. We wish to include the effect of the electric field or transverse magnetic field on depolarization, so we write the dipole-dipole Hamiltonian in this new basis for both spins.

Since the flip-flop processes are now of the form $|0,\pm\rangle\langle\pm,0|$, we redefine the η factor as

$$\eta^2 = \frac{1}{3}\left|\langle\pm,0|\frac{\mathcal{H}_{\rm dd}}{J_0/r^3}|0,\pm\rangle\right|^2 \frac{4\gamma_f^2}{(\omega_f - \omega_{\text{N-}V})^2 + 4\gamma_f^2}. \quad (10)$$

In the basis $\{|-\rangle, |0\rangle, |+\rangle\}$, the spin operators are

$$S_x = \begin{pmatrix} 0 & 1 & 0 \\ 1 & 0 & 0 \\ 0 & 0 & 0 \end{pmatrix}, \quad S_y = \begin{pmatrix} 0 & 0 & 0 \\ 0 & 0 & 1 \\ 0 & 1 & 0 \end{pmatrix},$$
$$S_z = \begin{pmatrix} 0 & 0 & 1 \\ 0 & 0 & 0 \\ 1 & 0 & 0 \end{pmatrix}. \quad (11)$$

The symmetry in the x-y plane is broken by the presence of the transverse electric or magnetic field. The x_i direction is defined as the direction of the transverse electric or magnetic field that dominates the single-spin Hamiltonian of particle i.

We consider two cases. (i) The x direction is defined by an external field (transverse magnetic field or strong external electric field) projected on the x-y plane of each class. In particular, this means that two spins from the same class have the same $(\hat{x},\hat{y},\hat{z})$ basis. (ii) The x direction is defined by the local electric field generated by the charges in the crystal. The correlation between $\hat{x}_1$ and $\hat{x}_2$ will then depend on the typical correlation length, l_c, of the local electric field and the average distance, d, between N-V and the fluctuator. If we assume $l_c \gg d$, we are back to the precedent case: $\hat{x}_1 = \hat{x}_2$. On the other hand, if we assume $l_c \ll d$, there is no correlation between $\hat{x}_1$ and $\hat{x}_2$. Numerically, this means that the spatial averaging of η will include an additional sampling of the relative angle, $\psi \in [0, 2\pi]$, between $\hat{x}_1$ and $\hat{x}_2$.

For these two cases, which we refer to as $\hat{x}_1 = \hat{x}_2$ and $\hat{x}_1 \neq \hat{x}_2$, we can compute the $\bar{\eta}$ factor in the three scenarios discussed previously, namely, $\widehat{z_1 z_2} = 0$ (same class), $\widehat{z_1 z_2} = 70.5°$, and $\widehat{z_1 z_2} = 109.5°$. The results, as well as those in the $|\pm1\rangle$ basis, are presented in Table III.

When $\mathbf{B} \perp [111]$ and $|\mathbf{B}| > 100$ G, the eigenbasis of the relevant class is $\{|0\rangle, |+\rangle, |-\rangle\}$. This class is spectrally isolated from the three others. The large amplitude of the magnetic field also ensures that the double-flip processes are quenched (see Sec. II E). We employ this geometry to determine the role of the electric field in depolarization at zero field experimentally. Under these assumptions, we find $\bar{\eta}^2 = 4\,\bar{\eta}_0^2$ in the case of $\hat{x}_1 = \hat{x}_2$.

TABLE III. $\frac{\bar{\eta}}{\frac{1}{4}\times\sqrt{\frac{1}{3}}}$ for the different eigenbases of the single-spin Hamiltonian, and for the different angles between the z axes of the two spins.

$\bar{\eta}$ table	$\widehat{z_1 z_2} = 0$	$\widehat{z_1 z_2} = 70.5°$	$\widehat{z_1 z_2} = 109.5°$
$\|\pm1\rangle$ basis	$\frac{2}{3\sqrt{3}} = 0.38$	0.65	0.83
$\|+/-\rangle$ basis $\hat{x}_1 \neq \hat{x}_2$	0.71	0.68	0.68
$\|+/-\rangle$ basis $\hat{x}_1 = \hat{x}_2$	$\frac{4}{3\sqrt{3}} = 0.77$	0.70	0.70

E. Double-flip processes

Double flips, or flip flips, are processes where the dipole-dipole interaction leads to flipping of both spins in the same direction. This is in contrast to flip-flops, where the two spins are flipped in opposite directions. These processes are more efficient if the coupled states have similar energies. To illustrate this, Fig. 6 depicts the energy levels of several tensor-product states $|i,j\rangle$, with no magnetic field. $|i\rangle$ denotes the electronic spin state of an N-V center, whereas $|j\rangle$ is the state of a fluctuator. When $B = 0$, four levels are resonant, and so, the dipolar interaction also allows efficient DF processes, as indicated by the red arrows.

We focus here on the main bases introduced earlier, namely, the $\{|0\rangle, |+1\rangle, |-1\rangle\}$ and $\{|0\rangle, |+\rangle, |-\rangle\}$ bases, and consider that the two spins are in the same eigenbasis (up to a rotation in the x-y plane for the $|\pm\rangle$ basis). The matrix elements of the dipole-dipole Hamiltonian involving double flips are thus $|0,\pm1\rangle\langle\mp1,0|$ and $|\pm1,0\rangle\langle0,\mp1|$

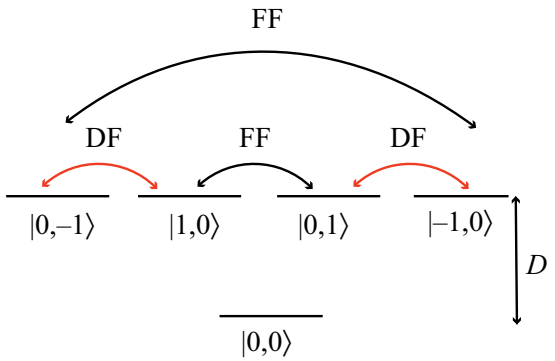

FIG. 6. Energy levels of the five lowest-energy tensor-product states. In the tensor product $|i,j\rangle$, the first part denotes the electronic spin state of an N-V center, whereas the second part is the state of a fluctuator. Arrows and the FF and DF notations indicate flip-flop and double-flip processes in the dipolar interaction, respectively. Note that, although the interaction is written in the eigenstate basis $\{|1\rangle, |0\rangle, |-1\rangle\}$ here, FF and DF also couple the states $|\pm,0\rangle$ and $|0,\pm\rangle$.

if the spin eigenbasis is $\{|0\rangle, |+1\rangle, |-1\rangle\}$, and $|0,\pm\rangle\langle\mp,0|$ and $|\pm,0\rangle\langle 0,\mp|$ if the spin eigenbasis is $\{|0\rangle, |+\rangle, |-\rangle\}$.

The double-flip processes will only be efficient if the splitting between the $|+1\rangle$ and $|-1\rangle$ states of the N-V center is comparable to the fluctuator linewidth. To compute the expected decay rate, we set a value for the splitting, $\Delta\nu$, between the $|+1\rangle$ and $|-1\rangle$ states, as well as for the combined width, σ, of the N-V and fluctuator spin transitions. We, in fact, only need to fix the ratio $\Delta\nu/\sigma$. As we show in Sec. III B, these two values are close to each other, so we make the approximation $\Delta\nu \approx \sigma$ in the following.

Under these assumptions, the $4\gamma_f^2/((\omega_f-\omega_{\text{N-}V})^2+4\gamma_f^2)$ factor in Eqs. (7) and (10) averages to a value of 1/2. We can then compute the $\bar{\eta}$ factors, similarly to when obtaining the results given in Table III, where η is now

$$\eta^2 = \frac{1}{3}\left|\langle\pm,0|\frac{\mathcal{H}_{dd}}{J_0/r^3}|0,\pm\rangle\right|^2 + \frac{1}{6}\left|\langle\pm,0|\frac{\mathcal{H}_{dd}}{J_0/r^3}|0,\mp\rangle\right|^2. \tag{12}$$

The results of the spatial averaging of Eq. (12) are shown in Table IV. Using these values, we can finally compute the depolarization rate in two experimentally relevant cases. (i) For $\mathbf{B}=0$, all four classes are degenerate and the spin eigenbasis is $|+/-\rangle$. This yields $\bar{\eta}^2 \approx 93.7\,\bar{\eta}_0^2$ for $\hat{x}_1 \neq \hat{x}_2$ and $\bar{\eta}^2 \approx 95.4\,\bar{\eta}_0^2$ for $\hat{x}_1 = \hat{x}_2$. (ii) For $\mathbf{B} \perp [111]$ and $|\mathbf{B}| = 20$ G, the relevant class is spectrally isolated from the other classes and its eigenbasis is $|+/-\rangle$. The splitting, $\Delta\nu$, between the $|+\rangle$ and $|-\rangle$ states still verifies $\Delta\nu \approx \sigma \approx 8$ MHz. This yields $\bar{\eta}^2 \approx 6.2\,\bar{\eta}_0^2$ for $\hat{x}_1 \neq \hat{x}_2$ and $\bar{\eta}^2 \approx 6.5\,\bar{\eta}_0^2$ for $\hat{x}_1 = \hat{x}_2$.

Our theoretical analysis gives a guideline for the expected changes in the T_1 times of the N-V centers under different magnetic field directions. Importantly, we see that double flips increase $\bar{\eta}$, so the spin-relaxation rate will increase significantly at zero field.

Let us now summarize all of our theoretical findings.

(1) The dipole-induced spin decay is lowest for a spectrally isolated class of N-V centers when the transverse magnetic field is negligible. In this case, the dipole-dipole relaxation is limited by flip-flop processes between spins of the same class. We call the corresponding stretched lifetime $T_1^{dd} \equiv T_0$.

TABLE IV. Computation of $\frac{\bar{\eta}}{\frac{1}{4}\times\sqrt{\frac{1}{3}}}$, including both flip-flop and double flips, for the different eigenbases of the single-spin Hamiltonian and for different angles between the z axes of the two spins.

$\bar{\eta}$ table	$\widehat{z_1z_2}=0$	$\widehat{z_1z_2}=70.5°$	$\widehat{z_1z_2}=109.5°$
$\|\pm1\rangle$ basis	0.87	0.93	1.00
$\|+/-\rangle$ basis $\hat{x}_1 \neq \hat{x}_2$	0.96	0.92	0.92
$\|+/-\rangle$ basis $\hat{x}_1 = \hat{x}_2$	0.98	0.92	0.92

(2) When a magnetic field is applied along the [100] axis (for 5 G $< |\mathbf{B}| \ll D/\gamma_e$), all four classes are resonant and their N-V eigenstates are, to a good approximation, the same as if a longitudinal magnetic field were applied. This results in an increase of the average flip-flop rate compared to the isolated class case. The predicted stretched exponential lifetime is $T_1^{dd} \approx T_0/42.8$.

(3) For a single spectrally isolated class in a transverse $\mathbf{B}$ field, where $\gamma_e B_\perp \ll D$, the change in the eigenstates of the single-particle Hamiltonian results in an increase of the average flip-flop rate. In the presence of an electric field, this leads to a new theoretical stretched lifetime: $T_1^{\text{dd}} = T_0/4$. When including both the role of the electric field and the double-flip processes, we obtain $T_1^{dd} \approx T_0/6.5$.

(4) For $\mathbf{B}$=0, all four classes are resonant with each other, the single-particle Hamiltonian of each spin is dominated by a random local electric field, and double flips are allowed. This results in an expected stretched lifetime: $T_1^{dd} \approx T_0/95$.

These assertions are now all tested experimentally.

III. SPIN-DEPOLARIZATION EXPERIMENTAL RESULTS

The first signatures of strong dipolar interactions can be seen quite straightforwardly by scanning a magnetic field and monitoring the N-V photoluminescence. Before showing a more detailed study of T_1 relaxation, we thus present such measurements for two diamond samples containing a low and high concentration of N-Vs. Figures 7(a) and 7(b) show the change in PL as a function of magnetic field using CVD-1 and HPHT-150-1. In both samples, we see a decrease in PL as the magnetic field amplitude increases. This can be understood as a mixing of the N-V states by the component of the magnetic field that is transverse with respect to the four N-V axes. There is, however, a stark difference in the low-magnetic-field region where only high-density samples show a drop in PL [22,23].

This effect is attributed to cross relaxation between the N-V centers through dipole-dipole coupling [23,28], at the root of which is a reduction of the spin T_1 time.

A. T_1 measurement

Figure 7(c) shows the sequence employed for measuring T_1^{dd}. It consists of a pump-probe measurement, where the spins are first polarized in the $|0\rangle$ state by a green laser and read-out optically after a variable dark time, τ. In highly doped samples, this sequence often results in artifacts, mostly due to charge-state transfer in the dark [28–30]. It is therefore convenient to repeat the sequence with an additional π pulse on one of the eight N-V spin resonances right before spin read-out to prepare the remaining $|0\rangle$ polarization in a darker $|+1\rangle$ or $|-1\rangle$ state [23,28,31]. By subtracting the result of the two sequences, we select

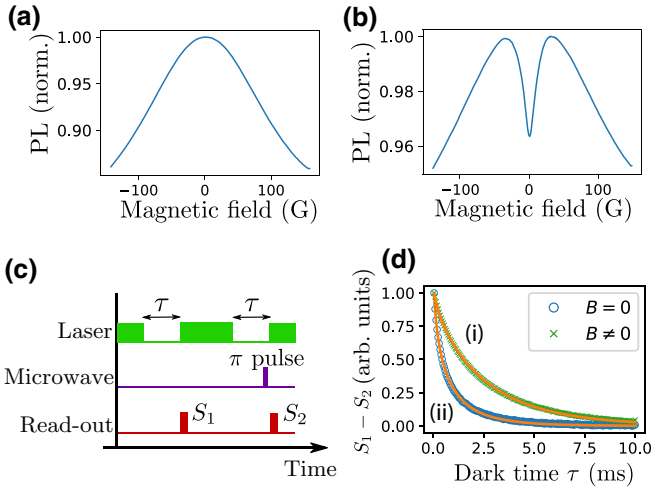

FIG. 7. (a),(b) Photoluminescence from N-V-center ensembles as a function of a magnetic field applied in an arbitrary direction for sample CVD-1 with [N-V^-]≈ 50 ppb and for sample HPHT-150-1 with [N-V^-]≈ 3 ppm, respectively. (c) Sequence used to measure the spin lifetime. (d) Traces (ii) and (i) are the spin-relaxation signals, $S_1 - S_2$, measured for sample HPHT-150-1 at zero and nonzero magnetic fields, respectively. Fitting procedure (orange plain line) is described in the text.

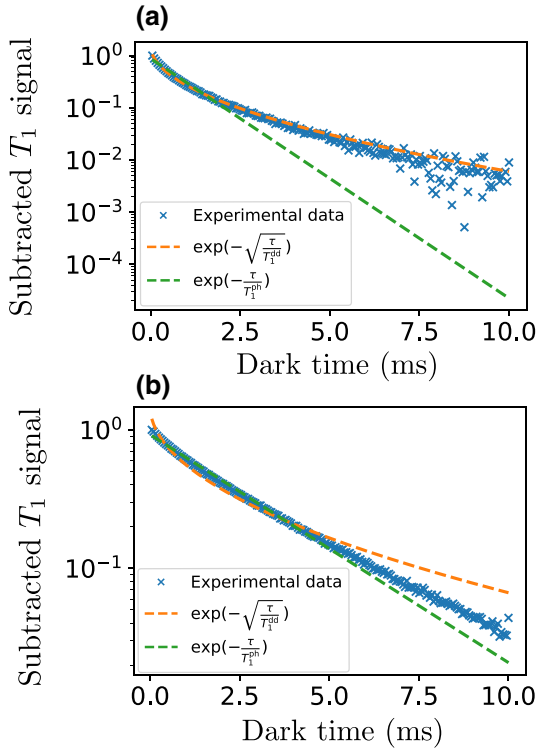

FIG. 8. T_1 measurement on a logarithmic scale, with purely exponential and purely stretched exponential fits (a) in zero magnetic field (b) in nonzero magnetic field. Sample HPHT-150-1.

only the spin-dependent part of the signal, with the added benefit of being able to select a specific class of N-V center. Traces (ii) and (i) in Fig. 7(d) are the spin-relaxation data obtained at zero and nonzero magnetic fields, respectively ($B \approx 50$ G). We see that the relaxation rate is significantly increased in zero magnetic field, which is unexpected for a phonon-dominated relaxation.

All dense samples used in this study, in fact, show $T_1^{dd} \sim T_1^{\text{ph}}$, where T_1^{ph} is the decay time due to phonons, so both decay processes are included in the analysis. Fitting the two traces of Fig. 7(d) to the product of a simple and a stretched exponential, we find $T_1^{\text{ph}} = 3.6$ ms for both curves and $T_1^{dd} = 0.6$ ms and 13.0 ms for traces (ii) and (i), respectively. These results thus demonstrate a 20-fold increase in the dipolar depolarization rate when the B field becomes zero. Figure 8 shows the result of a lifetime measurement, where $B = 0$ and $B = 50$ G in a direction for which every classes are split, on sample HPHT-150-1. In the fits, either purely exponential or purely stretched exponential functions are employed. We can see that the experimental data are better fitted by the stretched exponential profile when $B = 0$, whereas for $B = 50$ G, the experimental data follow the exponential profile more closely. To describe both regimes simultaneously, both T_1^{dd} and T_1^{ph} times have to be taken into account.

Of relevance to this study are the stretched exponential parts of the lifetime decay. Since the phonon-limited exponential decay does not depend on the external magnetic field, the value of T_1^{ph} for each sample can be fixed, which reduces the number of free parameters. The value found for all T_1 measurements on samples HPHT-150-1 and HPHT-150-2 are $T_1^{\text{ph}} = 3.62$ ms. Another more naive possibility to fit our T_1 measurements is the use a varying stretched factor, β, in the fitting function, such that

$$S(\tau) = A \exp\left(-\left(\frac{\tau}{T_1}\right)^{\beta}\right). \tag{13}$$

Figure 9 shows the optimal β parameter as a function of the external magnetic field on sample HPHT-150-1, which confirms that the T_1 profile gets closer to a purely stretched exponential in zero magnetic field, where dipolar interactions are the strongest. This procedure strengthens the need for a fit consisting of the product of a simple exponential and a stretched exponential with $\beta = 0.5$.

To further verify the validity of the fluctuator model in our experiment, we now study the spectral range of the dipolar relaxation.

B. Spectral range of the dipole-dipole cross relaxations

An experimental signature of the fluctuator hypothesis developed in Ref. [28] is the dependence of the depolarization rate when two near-resonant classes are brought to resonance: if there are indeed very fast decaying N-V

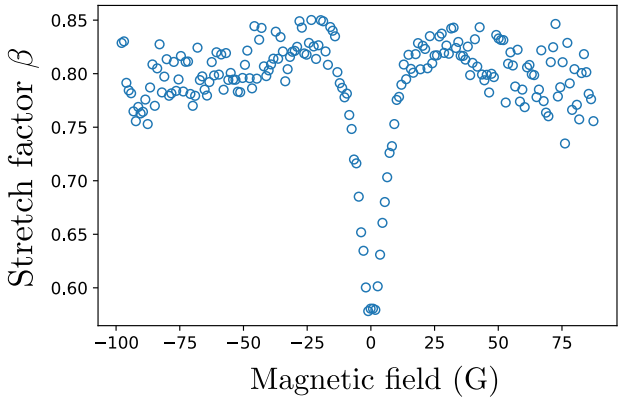

FIG. 9. Best stretch factor, β, for a T_1 fit of the form $f(\tau) = A\exp\left(-(\frac{\tau}{T_1})^{\beta}\right)$ as a function of an arbitrarily oriented magnetic field amplitude. Sample HPHT-150-1.

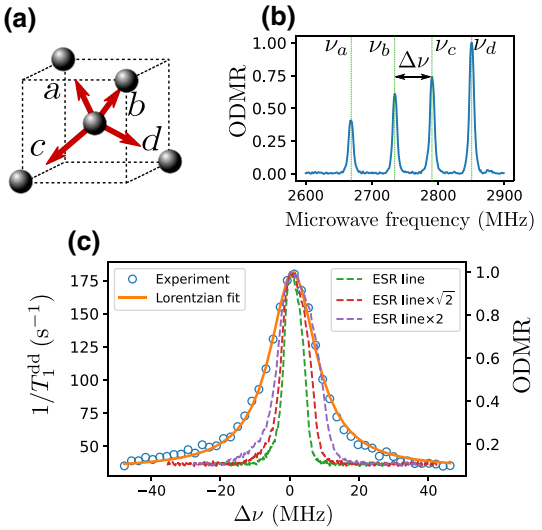

FIG. 10. Dipole-dipole depolarization for two near-resonant classes. (a) Sketch of the four possible N-V orientations ("classes") in a single diamond. (b) ODMR spectrum showing four $|0\rangle \rightarrow |-1\rangle$ resonances corresponding to the four spin classes. Detuning $\Delta\nu$ between classes b and c was controlled by changing the orientation of the external magnetic field. (c) Stretched part of the lifetime decay curve for the spins resonant with ν_c as a function of detuning $\Delta\nu$ (blue circles), fitted by a Lorentzian with a half width at half maximum of 8.0 MHz. Single-class ESR lines stretched by a factor of $1,\sqrt{2}$ and 2 are added for comparison. Sample HPHT-150-2.

centers (fluctuators with lifetime $T_1^f < 100$ ns), then the spectral width of the fluctuator would be greater than $1/T_2^*$. It is reasonable to assume that the latter is similar for all spins in the crystal, meaning that N-V centers exchange spin quanta (flip-flops) with nonresonant N-V fluctuators detuned by $\Delta\nu$, such that $2\pi/T_1^f > \Delta\nu > 2\pi/T_2^*$.

To verify this, we measure the spectral overlap between two classes, which, in the absence of a fluctuator, should be on the order of $1/T_2^*$, and compare it to the actual width of the depolarization rate of the spins as a function of detuning.

Figure 10 shows the results of such an experiment. The stretched part of the N-V decay rate is measured for each detuning in Fig. 10(c), which shows that $1/T_1^{dd}(\Delta\nu)$ is very well fitted by a Lorentzian with a half width of $\sigma = 8.0$ MHz. Note that this value of σ is not related to the direct coherent dipole–dipole-interaction-induced splitting: for a sample with 3 ppm of N-V centers, the average dipole–dipole-interaction strength between two nearest N-V centers is $J_0/r^3 \sim 27$ kHz, which is several orders of magnitude lower than σ.

In Fig. 10, we compare σ to the width of the ODMR line of a single class of N-V centers and to the overlap of two ODMR profiles. The spectral overlap, $S(\Delta\nu)$, between two spins of spectral response $S_1(\nu)$ and $S_2(\nu)$, centered, respectively, on the frequencies ν_1 and ν_2, is

$$S(\Delta\nu) = \int S_1(\nu,\nu_1)S_2(\nu,\nu_2)d\nu, \tag{14}$$

where $\Delta\nu = \nu_2 - \nu_1$. To approximate the spectral overlap of two ODMR signals, we consider the analytical solution in the Gaussian and Lorentzian cases. For two Gaussians of standard deviation σ, the spectral overlap as a function of detuning $\Delta\nu = \nu_1 - \nu_2$ is itself a Gaussian of standard deviation $\sigma' = \sqrt{2}\sigma$. Indeed,

$$S(\Delta\nu) \propto \int \exp\left(-\frac{(\nu-\nu_1)^2}{2\sigma^2}\right)\exp\left(-\frac{(\nu-\nu_2)^2}{2\sigma^2}\right)d\nu$$
$$\propto \exp\left(-\frac{(\Delta\nu)^2}{4\sigma^2}\right).$$

For two Lorentzian profiles with widths σ, the overlap function is

$$S(\Delta\nu) \propto \int \frac{1}{1+\frac{(\nu-\nu_1)^2}{\sigma^2}}\cdot\frac{1}{1+\frac{(\nu-\nu_2)^2}{\sigma^2}}d\nu$$
$$\propto \frac{1}{1+\frac{(\Delta\nu)^2}{4\sigma^2}}.$$

It is thus also a Lorentzian with a width of $\sigma' = 2\sigma$. Although most ODMR profiles are close to Gaussian, some are neither purely Lorentzian nor purely Gaussian. The trend depends on the employed sample. The overlap between two classes can thus be approximated by a single-class ODMR profile stretched by a factor ranging between $\sqrt{2}$ and 2.

In Fig. 10, not only is the width of the function $(1/T_1^{dd})(\Delta\nu)$ significantly larger than the overlap of

ODMR spectra of two N-V centers, it also agrees very well with a Lorentzian profile. This observation is in agreement with a fluctuator model, where the latter is supposed to have a very short lifetime, related to its spectral width by Fourier transform.

C. Relaxation for two different magnetic field directions with identical degeneracy

One of the findings of our theoretical study is that degeneracy is not the sole parameter that determines relaxation. We indeed identified a regime where relaxation differed for two different B-field directions, while the microwave selected two degenerate N-V classes in both cases.

When the magnetic field lies in the {100}-crystalline-plane family, where the angle $\widehat{z_1 z_2} = \arccos(1/3) \approx 70.5°$, numerical simulations yield $\bar{\eta}_{\text{close}} \approx 1/4 \times \sqrt{1/3} \times 0.65$. On the other hand, when the magnetic field lies in the {110}- or $\{1\bar{1}0\}$-crystalline-plane family, where $\widehat{z_1 z_2} = \arccos(-1/3) \approx 109.5°$, numerical simulations give $\bar{\eta}_{\text{far}} \approx 1/4 \times \sqrt{1/3} \times 0.83$ (see Table I). Figure 11(a) shows a graphical representation of the difference between the two scenarios: due to the $\mathbf{B} \cdot \hat{z} > 0$ condition, the same two classes of N-V centers can have a $\widehat{z_1 z_2}$ angle equal to 70.5° or 109.5°, depending on the external magnetic field.

These computed values can be tested experimentally. Figure 11(b) shows the T_1 signal measured on the same sample, HPHT-15-2, for eight different values of the magnetic field, where the microwave is tuned to a two-class resonance. In the first four cases, the magnetic field lies in one of the {100} planes, and in the four other cases, it is in one of the {110} planes. We can see that the measured lifetime is always smaller in the {110} case, which corresponds the greater $\bar{\eta}$ factor computed previously.

This finding not only shows the accuracy of the theoretical treatment described in Sec. II, but it also highlights the fact that degeneracy is not the sole parameter governing spin relaxation.

D. Relaxation in zero field

The fluctuator model developed in Ref. [28] contains some of the explanations for the increase in dipolar depolarization that we observed at zero field in Figs. 7 and 8. All four N-V classes in the diamond are resonant in zero field, which increases the flip-flop rates, as opposed to when the magnetic field lifts some degeneracies. However, the extra specificities of the zero-magnetic-field region, namely, the role of the local electric field and double-flip processes are seen to play a role in the theoretical modeling presented in Sec. II.

To decipher the role played by these interactions, one requires a dedicated experimental setting. Figures 12(a) and 12(b-i) show ODMR spectra with and without a magnetic field, from the dense ensemble HPHT-150-1. Using

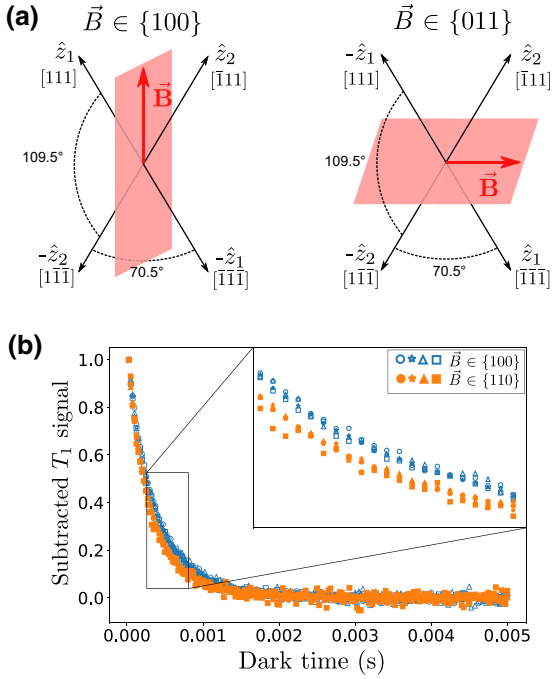

FIG. 11. (a) Geometrical representation of two N-V classes, and the two possible planes where the magnetic field has the same projection on both classes. Positive $\hat{z}_i$ direction is chosen so that $\mathbf{B} \cdot \hat{z}_i > 0$. (b) T_1 measurement on a two-class resonance. Eight different magnetic field angles were employed on the same sample: 4 times in the {100} plane (blue unfilled symbols) and 4 times in the {110} plane (orange filled symbols). Inset, magnification of the 0.3–0.8-ms region. Sample HPHT-150-2.

the same magnetic field alignment, Figs. 12(b-ii) and 12(b-iii) show the PL and the $1/T_1^{dd}$ decay rates from the N-V-center ensemble as a function of the amplitude of the magnetic field. We observe that the 4% increase in PL as the magnetic field increases is indeed associated with a drop in the spin-decay rate from 1600 s^{-1} to 80 s^{-1}. This result can again be explained by the decreasing number of resonant spins as the zero magnetic field is increased. The half width of the dip ($\approx$ 10 G) is also consistent with the fluctuator model, taking into account the reduction of the two spin resonances overlapping as the B field is increased.

Figure 12(c-i) instead displays an ODMR where all four classes are resonant when scanning the magnetic field along one of the four [100] crystalline axes. The changes in PL and $1/T_1^{dd}$ are shown in Figs. 12(c-ii) and 12(c-iii) as a function of a magnetic field that is aligned in this direction. Note that the slight drop in PL and the corresponding bump for $1/T_1^{dd}$ at $B \sim 20$ G are related to the dipolar interaction with N-V centers that have ^{13}C as the first neighbor [17]. Most importantly, an increase in the spin-decay rate can still be observed, as well as a corresponding drop in PL when the magnetic field tends to zero. Since all classes are always resonant, flip-flop cannot be the cause of the

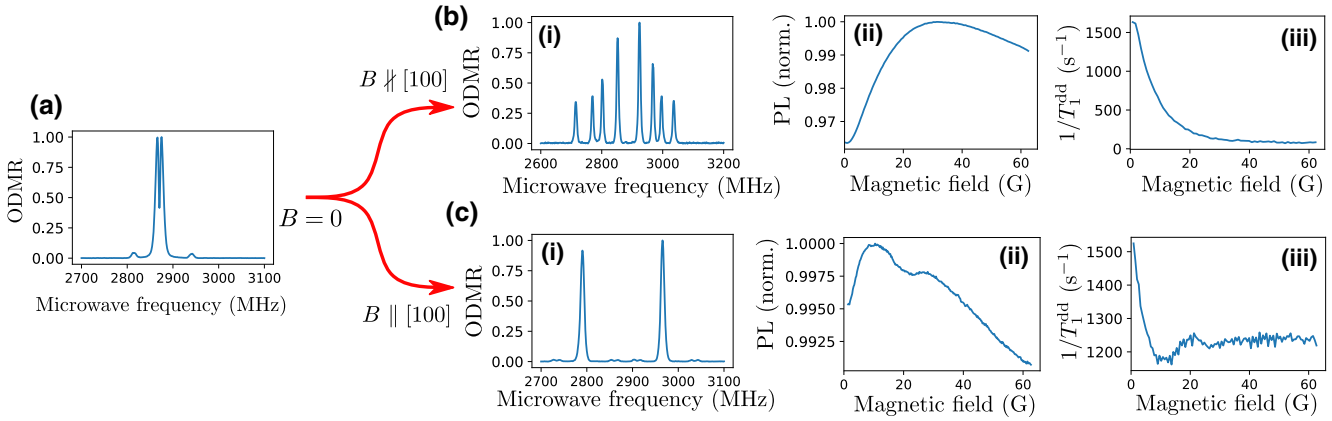

FIG. 12. (a) ODMR spectrum in zero field with microwave-amplitude modulation. (b-i) ODMR spectrum for a magnetic field approximately equal to 60 G, misaligned by about 24° from the [100] axis. (b-ii) Normalized PL of the N-V^- ensemble as a function of the magnetic field amplitude. (b-iii) Stretched part of the spin decay, $1/T_1^{dd}$, as a function of the magnetic field amplitude. (c-i)–(c-iii) Same measurements as in (b) but with a magnetic field close to the [100] axis. All the measurements were realized using the sample HPHT-150-1.

change in spin relaxation in this experiment. PL and $1/T_1^{dd}$ changes with **B** field are also much sharper in this scenario.

This effect points towards the role played by other terms than flip-flops in the dipolar Hamiltonian. One of the differences between scans in the [100] and arbitrary directions is the critical magnetic field amplitude required to lift the degeneracy of the four classes. Figure 13(a) shows the simulated energies of the four $|0\rangle \rightarrow |-1\rangle$ and four $|0\rangle \rightarrow |+1\rangle$ transitions as a function of the magnetic field, in the magnetic field alignment employed in Fig. 12(b). Figure 13(b) shows the difference in energy between the closest pairs of transitions. We can see that the energy detuning, $\Delta\nu$, between classes crosses the value of the dipole–dipole-interaction range for magnetic field values, $|\mathbf{B}|$, in the 12–15-G range. These values are close to the half width of the zero-field feature in Figs. 12(b-ii) and 12(b-iii). When $|\mathbf{B}| \gg 20$ G, the only resonant terms

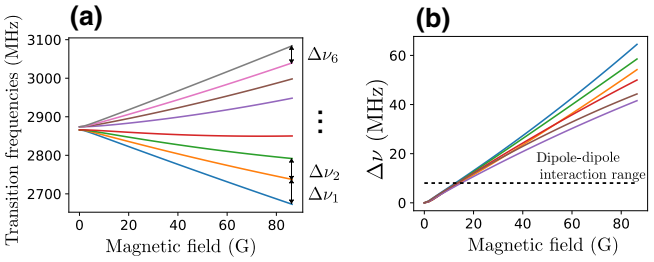

FIG. 13. (a) Simulation showing the eight possible transition frequencies (four $|0\rangle \rightarrow |-1\rangle$ and four $|0\rangle \rightarrow |+1\rangle$ transitions) as a function of the magnetic field amplitude for the orientation of the magnetic field shown in Fig. 12(b). (b) Difference in frequency between each pair of closest classes as a function of magnetic field amplitude. Dotted line at $\Delta\nu = 8.04$ MHz corresponds to an estimation of the dipole–dipole-interaction frequency range.

in the dipole-dipole coupling between N-V centers are the flip-flop terms $|0, \pm 1\rangle \langle \pm 1, 0|$. The half width of the zero-field feature when the B field is scanned along the [100] direction (≈ 2 G) is, however, consistent with $d_\perp E_\perp \approx 3.3$ MHz.

To claim that the decrease in PL at low magnetic field in Fig. 12(c-ii) is due to the local electric field and the double-flip processes, one should ensure that there is no misalignment of the magnetic field with respect to the [100] axis, as it is scanned. The four classes could, for instance, be truly resonant only with zero external magnetic field and not resonant when the B field is large.

Figure 14 shows the change in PL with respect to the external magnetic field amplitude for various misalignments of the magnetic field direction with respect to the [100] diamond crystalline axis of the sample CVD-2. The initial alignment of the magnetic field was controlled by applying a field of about 50 G and monitoring the overlap of the four classes with ODMR spectra (maximizing

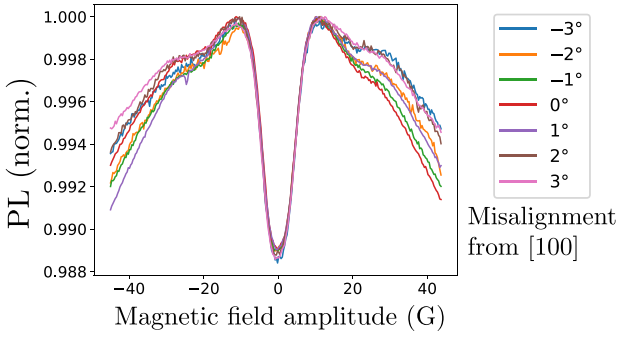

FIG. 14. PL of sample CVD-2 as a function of the external magnetic field amplitude for different magnetic field misalignments with respect to the [100] axis.

the PL drop is also an effective method). The initial alignment precision is estimated to be $\pm 1^{\circ}$. The misalignment was then introduced by rotating the electromagnet along an arbitrary axis. We can see that the central drop in PL is not critically affected by the misalignment of the magnetic field, and we are therefore confident that the drop in PL we observe in Figs. 12(c-ii) and 12(c-iii) is not due to misalignment of the magnetic field angle from the [100] axis. Note that the slight asymmetry between the positive and negative values of the magnetic field could come from the Earth's magnetic field or from hysteresis in the magnetic core of our electromagnet.

Our experiments, together with the simulations, suggest that electric fields and double-flips should play a significant role at zero field. Separating the two processes experimentally, however, requires further analyses, which we provide in Sec. III E.

E. Separating the role of double flips and electric field in zero-field relaxation

To estimate the respective role of double flips and electric field in zero field, we resort to an extra feature of the electric field Hamiltonian, which is the robustness of its eigenstates under transverse B field. As discussed in Sec. I, when $B_{\perp} \leq 150$ G, the eigenstates of the spin Hamiltonian are close to $|0\rangle$, $|+\rangle$, and $|-\rangle$ to about 2%. Crucially, for $B_{\perp} = 150$ G, the splitting, $\Delta\nu$, between the $|+\rangle$ and $|-\rangle$ states is equal to about 70 MHz, almost an order of magnitude greater than the fluctuator linewidth. This means that we can effectively quench the double flips by splitting the $|+\rangle$ and $|-\rangle$ states. The transverse field can thus be used to emulate the role of the electric field, a property that has previously been employed to increase the electric-field-sensing ability of N-V centers [32,33].

Figure 15(a) shows an ODMR spectrum where $B_{\perp} = 20$ G on the HPHT-150-2 sample. The central two lines correspond to the $|0\rangle \rightarrow |-\rangle$ and $|0\rangle \rightarrow |+\rangle$ transitions for the class that is orthogonal to **B**. Figure 15(c) shows the measurement of the decay rate, $1/T_1^{dd}$, for that class, as a function of $B_{\perp}$. Two regions can be observed on this graph: in region A, the decay rate decreases with $B_{\perp}$, while in region B it stabilizes to a value of $1/T_1^{dd} = (60 \pm 5)\ \mathrm{s}^{-1}$. We also indicated the value of $1/T_1^{dd} = (25 \pm 5)\ \mathrm{s}^{-1}$ found for the same class but employing a longitudinal magnetic field.

To understand these results, we plot detuning $\Delta\nu$ between the states $|+\rangle$ and $|-\rangle$ as a function of $B_{\perp}$ in Fig. 15(b). When $\Delta\nu \leq 20$ MHz (region A), both double flips and flip-flops are efficient, but when $\delta\nu \gg 20$ MHz (region B), double flips are quenched and only flip-flop processes remain. We note that the decay rate in the $\{|0\rangle, |\pm\rangle\}$ basis is more than twice as large as the decay rate coming from intraclass flip-flops in the $\{|0\rangle, |\pm 1\rangle\}$ basis in region B. This effect is corroborated by our model.

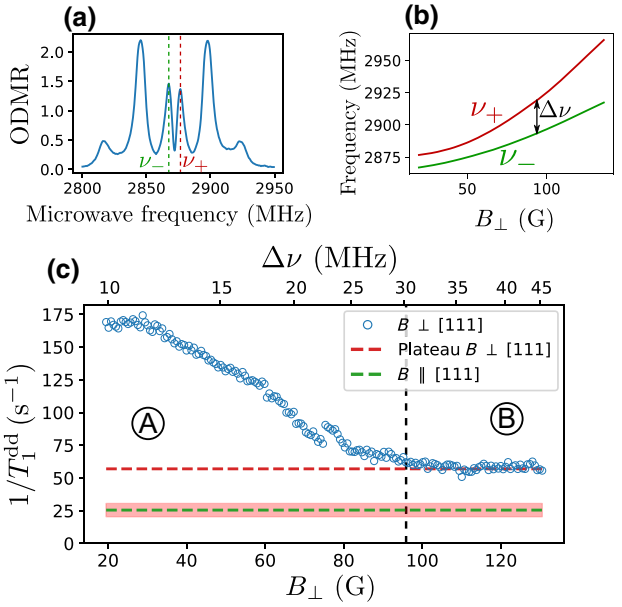

FIG. 15. (a) ODMR spectrum for $B_{\perp} = 20$ G. Two transition frequencies of the class that is orthogonal to B are denoted ν_+ and ν_-. (b) Measurement of ν_+ and ν_- through ODMR as a function of $B_{\perp}$. (c) Measurement of $1/T_1^{dd}$ for a single N-V class as a function of $B_{\perp}$. Red dashed line is the value reached for high transverse field. Green dashed line corresponds to the value found for the same sample and N-V class, under a longitudinal magnetic field. Error bars are depicted by the shaded pink region. Detuning $\Delta\nu = \nu_+ - \nu-$ is indicated on the top x axis. Vertical black dashed line indicates the separation between regions A and B. Sample HPHT-150-2.

Importantly, in region A, the double-flip processes give a maximum decay rate that is about 5 times greater than the decay caused by the change of basis alone. From these results, and according to our model, the double flips are thus the dominant cause of zero-field depolarization observed in Fig. 12(c-iii).

IV. LOW-FIELD MAGNETOMETRY PROTOCOL

Our observations have important implications for magnetometry with N-V ensembles. Dc microwave-free magnetometry has already been performed using either N-V–N-V cross relaxations [14,15] or level anticrossings [34–36]. Here, we propose a similar protocol but using spin depolarization at zero field. To do so, we use lock-in detection and add a magnetic field modulation at 1 kHz with an amplitude of about 10 G through the same electromagnet. Figure 16(a) shows the demodulated PL while a dc magnetic field is scanned in an arbitrary direction. Here, we use the HPHT-15-1 sample with a laser power of about 1 mW. The optical power in the collected PL is around 1 μW. We can see a sharp linear slope at low field, $|B| < 5$ G. Once calibrated, we have access to a one-dimensional magnetometer, which can be extended to

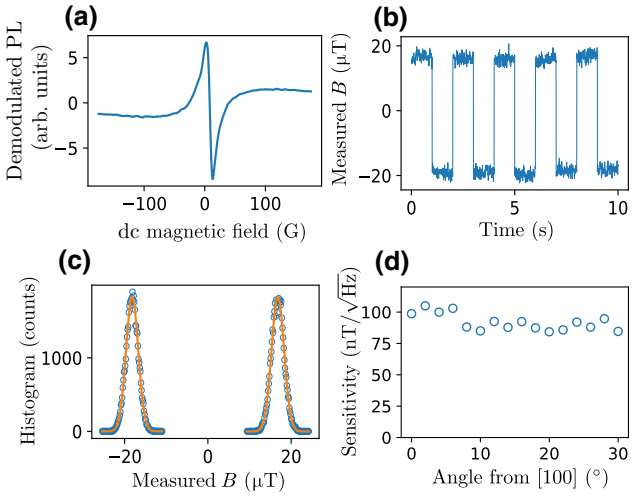

FIG. 16. Low-field magnetometry protocol. (a) Demodulated PL as a function of an externally applied magnetic field. (b) External magnetic field read-out. (c) Histogram of the measurement in (b) fitted by Gaussians of standard deviation $\sigma = 1.5\ \mu$T. (d) Measured sensitivity as function of the angle between the external magnetic field and the [100] crystalline axis. Sample HPHT-15-1.

three dimensions with a set of three coils or three electromagnets, as in Ref. [36]. To assess the sensitivity of the measurement, we alternate a small dc field of about 40 μT every few seconds and take a histogram of the measured fields (with a total duration of 50 s), as shown in Figs. 16(b) and 16(c). The histogram is well fitted by Gaussians of standard deviation $\sigma = 1.5\ \mu$T. The measurement was performed here with an output low-pass filter of time constant $\tau = 3$ ms, which gives us a dc sensitivity of $\eta = \sigma\sqrt{\tau} = 82\ n\text{T}/\sqrt{\text{Hz}}$. This value corresponds to $\eta/\sqrt{V} \approx 4.7\ \mu\text{T}/\mu\text{m}^{3/2}/\sqrt{\text{Hz}}$ when normalized to the volume. Importantly, this measurement is consistent with the experimentally found sensitivity of about $5\ \mu\text{T}/\sqrt{\text{Hz}}$ obtained with sample HPHT-1-1. Our results thus offer bright prospects for high-sensitivity magnetometry using N-V centers in millimeter-size volumes.

Compared to previously employed protocols, the sensitivity does not crucially depend on crystalline orientation, making this magnetometer principle operational with diamond powders or polycrystalline samples. Another significant advantage is that this measurement is insensitive to thermal fluctuations and strain inhomogeneities because dipolar relaxation at zero field does not depend on the zero-field splitting. In other typical N-V magnetometers, however, the zero-field-splitting dependence on temperature and strain can yield systematic errors [6,7]. We now evaluate the relative role of the three causes of spin depolarization that assist the operation of the magnetometer. To do so, we measure its sensitivity while changing the angle of the magnetic field. The results are shown in Fig. 16(d). We observe only about 10% improvement in the sensitivity as we leave the [100] region. When **B** ∥ [100], only the double flips and the electric field cause depolarization, whereas the three effects are at play in all the other orientations. It should be noted that this observation is sample dependent. Other samples, including those from the same batch, have shown higher orientational dependences, corresponding to a lower contribution from local electric fields and double-flip processes. Interestingly, here, the double flips and electric field effects are the dominant factors in the sensitivity of this protocol.

V. CONCLUSION

We identified three mechanisms causing spin depolarization in zero field for a dense ensemble of N-V^- centers, all related to an increase in the dipole–dipole-induced CR between the spins of N-V centers. The lift in degeneracy of the spin state of different N-V classes was found to be the main cause of zero-field depolarization, followed by double-flip processes, and then electric-field-induced mixing. We employed CR for microwave-free and orientation-free dc magnetometry and demonstrated sensitivities in the $\eta/\sqrt{V} \approx 5\ \mu\text{T}/\mu\text{m}^{3/2}/\sqrt{\text{Hz}}$ range for commercially available diamonds. We believe that our results are also useful for microwave-based low-field magnetometry [37,38], as well as for understanding many-body phenomena [8–11] and spin-mechanical effects [39] with strongly coupled spins.

ACKNOWLEDGMENTS

We would like to acknowledge support from Alexandre Tallaire and Jocelyn Achard as well as QUANTIP for funding.

[1] M. W. Doherty, N. B. Manson, P. Delaney, F. Jelezko, J. Wrachtrup, and L. C. Hollenberg, The nitrogen-vacancy colour centre in diamond, Phys. Rep. **528**, 1 (2013).

[2] V. M. Acosta, E. Bauch, M. P. Ledbetter, C. Santori, K.-M. C. Fu, P. E. Barclay, R. G. Beausoleil, H. Linget, J. F. Roch, F. Treussart, S. Chemerisov, W. Gawlik, and D. Budker, Diamonds with a high density of nitrogen-vacancy centers for magnetometry applications, Phys. Rev. B **80**, 115202 (2009).

[3] A. Tallaire, O. Brinza, P. Huillery, T. Delord, C. Pellet-Mary, R. Staacke, B. Abel, S. Pezzagna, J. Meijer, N. Touati, L. Binet, A. Ferrier, P. Goldner, G. Hetet, and J. Achard, High NV density in a pink CVD diamond grown with N2O addition, Carbon **170**, 421 (2020).

[4] A. M. Edmonds, C. A. Hart, M. J. Turner, P.-O. Colard, J. M. Schloss, K. S. Olsson, R. Trubko, M. L. Markham, A. Rathmill, B. Horne-Smith, Wilbur Lew, Arul Manickam, Scott Bruce, Peter G. Kaup, Jon C. Russo, Michael J. DiMario, Joseph T. South, Jay T. Hansen, Daniel J. Twitchen, and Ronald L. Walsworth, Characterisation of

CVD diamond with high concentrations of nitrogen for magnetic-field sensing applications, Mater. Quantum Technol. **1**, 025001 (2021).

[5] G. Chatzidrosos, J. S. Rebeirro, H. Zheng, M. Omar, A. Brenneis, F. M. Stürner, T. Fuchs, T. Buck, R. Rölver, T. Schneemann, Peter Blümler, Dmitry Budker, and Arne Wickenbrock, Fiberized diamond-based vector magnetometers, Front. Photonics **5**, 4 (2021).

[6] J. F. Barry, J. M. Schloss, E. Bauch, M. J. Turner, C. A. Hart, L. M. Pham, and R. L. Walsworth, Sensitivity optimization for N*V*-diamond magnetometry, Rev. Mod. Phys. **92**, 015004 (2020).

[7] E. Bauch, C. A. Hart, J. M. Schloss, M. J. Turner, J. F. Barry, P. Kehayias, S. Singh, and R. L. Walsworth, Ultralong dephasing times in solid-state spin ensembles via quantum control, Phys. Rev. X **8**, 031025 (2018).

[8] G. Kucsko, S. Choi, J. Choi, P. C. Maurer, H. Zhou, R. Landig, H. Sumiya, S. Onoda, J. Isoya, F. Jelezko, E. Demler, N. Y. Yao, and M. D. Lukin, Critical Thermalization of a Disordered Dipolar Spin System in Diamond, Phys. Rev. Lett. **121**, 023601 (2018).

[9] S. Choi, J. Choi, R. Landig, G. Kucsko, H. Zhou, J. Isoya, F. Jelezko, S. Onoda, H. Sumiya, V. Khemani, C. von Keyserlingk, N. Y. Yao, E. Demler, and M. D. Lukin, Observation of discrete time-crystalline order in a disordered dipolar many-body system, Nature **543**, 221 (2017).

[10] C. Zu, F. Machado, B. Ye, S. Choi, B. Kobrin, T. Mittiga, S. Hsieh, P. Bhattacharyya, M. Markham, D. Twitchen, A. Jarmola, D. Budker, C. R. Laumann, J. E. Moore, and N. Y. Yao, Emergent hydrodynamics in a strongly interacting dipolar spin ensemble, Nature **597**, 45 (2021).

[11] B. L. Dwyer, L. V. Rodgers, E. K. Urbach, D. Bluvstein, S. Sangtawesin, H. Zhou, Y. Nassab, M. Fitzpatrick, Z. Yuan, and K. De Greve *et al.*, Probing spin dynamics on diamond surfaces using a single quantum sensor, arXiv preprint arXiv:2103.12757 (2021).

[12] S. Choi, J. Choi, R. Landig, G. Kucsko, H. Zhou, J. Isoya, F. Jelezko, S. Onoda, H. Sumiya, V. Khemani, C. von Keyserlingk, N. Y. Yao, E. Demler, and M. D. Lukin, Observation of discrete time-crystalline order in a disordered dipolar many-body system, Nature **543**, 221 (2017), number: 7644 Publisher: Nature Publishing Group.

[13] H. Zhou, J. Choi, S. Choi, R. Landig, A. M. Douglas, J. Isoya, F. Jelezko, S. Onoda, H. Sumiya, P. Cappellaro, Helena S. Knowles, Hongkun Park, and Mikhail D. Lukin, Quantum metrology with strongly interacting spin systems, Phys. Rev. X **10**, 031003 (2020).

[14] R. Akhmedzhanov, L. Gushchin, N. Nizov, V. Nizov, D. Sobgayda, I. Zelensky, and P. Hemmer, Microwave-free magnetometry based on cross-relaxation resonances in diamond nitrogen-vacancy centers, Phys. Rev. A **96**, 013806 (2017), number: 1.

[15] R. Akhmedzhanov, L. Gushchin, N. Nizov, V. Nizov, D. Sobgayda, I. Zelensky, and P. Hemmer, Magnetometry by cross-relaxation-resonance detection in ensembles of nitrogen-vacancy centers, Phys. Rev. A **100**, 043844 (2019), number: 4.

[16] O. Dhungel, T. Lenz, M. Omar, J. Shaji Rebeirro, V. Ivady, A. Gali, A. Wickenbrock, and D. Budker, Zero-field microwave-free magnetometry with ensembles of nitrogen-vacancy centers in diamond, arXiv e-prints , arXiv:2301.09666 (2023).

[17] C. Pellet-Mary, P. Huillery, M. Perdriat, A. Tallaire, and G. Hétet, Optical detection of paramagnetic defects in diamond grown by chemical vapor deposition, Phys. Rev. B **103**, L100411 (2021).

[18] T. Wolf, P. Neumann, K. Nakamura, H. Sumiya, T. Ohshima, J. Isoya, and J. Wrachtrup, Subpicotesla diamond magnetometry, Phys. Rev. X **5**, 041001 (2015).

[19] F. M. Stürner, A. Brenneis, T. Buck, J. Kassel, R. Rölver, T. Fuchs, A. Savitsky, D. Suter, J. Grimmel, S. Hengesbach, M. Förtsch, K. Nakamura, H. Sumiya, S. Onoda, J. Isoya, and F. Jelezko, Integrated and portable magnetometer based on nitrogen-vacancy ensembles in diamond, Adv. Quantum Technol. **4**, 2000111 (2021).

[20] D. Filimonenko, V. Yasinskii, A. Nizovtsev, and S. Y. Kilin, Weak magnetic field resonance effects in diamond with nitrogen-vacancy centers, Semiconductors **52**, 1865 (2018).

[21] D. Filimonenko, V. Yasinskii, A. P. Nizovtsev, S. Y. Kilin, and F. Jelezko, Manifestation in IR-luminescence of cross relaxation processes between N*V*-centers in weak magnetic fields, J. Appl. Spectrosc. **88**, 1131 (2022).

[22] A. Jarmola, A. Berzins, J. Smits, K. Smits, J. Prikulis, F. Gahbauer, R. Ferber, D. Erts, M. Auzinsh, and D. Budker, Longitudinal spin-relaxation in nitrogen-vacancy centers in electron irradiated diamond, Appl. Phys. Lett. **107**, 242403 (2015), number: 24.

[23] M. Mrózek, D. Rudnicki, P. Kehayias, A. Jarmola, D. Budker, and W. Gawlik, Longitudinal spin relaxation in nitrogen-vacancy ensembles in diamond, EPJ Quantum Technol. **2**, 22 (2015), number: 1.

[24] R. Epstein, F. Mendoza, Y. Kato, and D. Awschalom, Anisotropic interactions of a single spin and dark-spin spectroscopy in diamond, Nat. Phys. **1**, 94 (2005).

[25] N. D. Lai, D. Zheng, F. Jelezko, F. Treussart, and J.-F. Roch, Influence of a static magnetic field on the photoluminescence of an ensemble of nitrogen-vacancy color centers in a diamond single-crystal, Appl. Phys. Lett. **95**, 133101 (2009).

[26] T. Mittiga, S. Hsieh, C. Zu, B. Kobrin, F. Machado, P. Bhattacharyya, N. Rui, A. Jarmola, S. Choi, D. Budker, and N. Y. Yao, Imaging the Local Charge Environment of Nitrogen-Vacancy Centers in Diamond, Phys. Rev. Lett. **121**, 246402 (2018).

[27] E. Van Oort and M. Glasbeek, Electric-field-induced modulation of spin echoes of N*V* centers in diamond, Chem. Phys. Lett. **168**, 529 (1990).

[28] J. Choi, S. Choi, G. Kucsko, P. C. Maurer, B. J. Shields, H. Sumiya, S. Onoda, J. Isoya, E. Demler, F. Jelezko, Norman Y. Yao, and Mikhail D. Lukin, Depolarization Dynamics in a Strongly Interacting Solid-State Spin Ensemble, Phys. Rev. Lett. **118**, 093601 (2017).

[29] R. Giri, F. Gorrini, C. Dorigoni, C. E. Avalos, M. Cazzanelli, S. Tambalo, and A. Bifone, Coupled charge and spin dynamics in high-density ensembles of nitrogen-vacancy centers in diamond, Phys. Rev. B **98**, 045401 (2018), number: 4.

[30] R. Giri, C. Dorigoni, S. Tambalo, F. Gorrini, and A. Bifone, Selective measurement of charge dynamics in an ensemble

of nitrogen-vacancy centers in nanodiamond and bulk diamond, Phys. Rev. B **99**, 155426 (2019), number: 15.

[31] A. Jarmola, V. M. Acosta, K. Jensen, S. Chemerisov, and D. Budker, Temperature- and Magnetic-Field-Dependent Longitudinal Spin Relaxation in Nitrogen-Vacancy Ensembles in Diamond, Phys. Rev. Lett. **108**, 197601 (2012), number: 19.

[32] F. Dolde, H. Fedder, M. W. Doherty, T. Nöbauer, F. Rempp, G. Balasubramanian, T. Wolf, F. Reinhard, L. C. Hollenberg, F. Jelezko, and J. Wrachtrup, Electric-field sensing using single diamond spins, Nat. Phys. **7**, 459 (2011).

[33] Z. Qiu, A. Hamo, U. Vool, T. X. Zhou, and A. Yacoby, Nanoscale electric field imaging with an ambient scanning quantum sensor microscope, arXiv preprint arXiv:2205.03952 (2022).

[34] A. Wickenbrock, H. Zheng, L. Bougas, N. Leefer, S. Afach, A. Jarmola, V. M. Acosta, and D. Budker, Microwave-free magnetometry with nitrogen-vacancy centers in diamond, Appl. Phys. Lett. **109**, 053505 (2016).

[35] H. Zheng, G. Chatzidrosos, A. Wickenbrock, L. Bougas, R. Lazda, A. Berzins, F. H. Gahbauer, M. Auzinsh, R. Ferber, and D. Budker, in *Slow Light, Fast Light, and Opto-Atomic Precision Metrology X*, Vol. 10119 (SPIE, San Francisco, California, USA, 2017), p. 115.

[36] H. Zheng, Z. Sun, G. Chatzidrosos, C. Zhang, K. Nakamura, H. Sumiya, T. Ohshima, J. Isoya, J. Wrachtrup, A. Wickenbrock, and D. Budker, Microwave-Free Vector Magnetometry with Nitrogen-Vacancy Centers along a Single Axis in Diamond, Phys. Rev. Appl. **13**, 044023 (2020), number: 4.

[37] P. J. Vetter, A. Marshall, G. T. Genov, T. F. Weiss, N. Striegler, E. F. Großmann, S. Oviedo-Casado, J. Cerrillo, J. Prior, P. Neumann, and F. Jelezko, Zero- and Low-Field Sensing with Nitrogen-Vacancy Centers, Phys. Rev. Appl. **17**, 044028 (2022).

[38] N. Wang, C.-F. Liu, J.-W. Fan, X. Feng, W.-H. Leong, A. Finkler, A. Denisenko, J. Wrachtrup, Q. Li, and R.-B. Liu, Zero-field magnetometry using hyperfine-biased nitrogen-vacancy centers near diamond surfaces, Phys. Rev. Res. **4**, 013098 (2022).

[39] C. Pellet-Mary, P. Huillery, M. Perdriat, and G. Hétet, Magnetic torque enhanced by tunable dipolar interactions, Phys. Rev. B **104**, L100411 (2021).